Self-regulated transport in photonic crystals with phase-changing defects

Roney Thomas,[1] Fred M. Ellis,[1] Ilya Vitebskiy,[2] and Tsampikos Kottos[1]
[1]*Department of Physics, Wesleyan University, 265 Church St., Middletown, Connecticut 06457, USA*
[2]*Air Force Research Laboratory, Sensors Directorate, Wright-Patterson Air Force Base, Ohio 45433, USA*

(Received 9 February 2017; published 4 January 2018)

Phase-changing materials (PCMs) are widely used for optical data recording, sensing, all-optical switching, and optical limiting. Our focus here is on the case when the change in transmission characteristics of the optical material is caused by the input light itself. Specifically, the light-induced heating triggers the phase transition in the PCM. In this paper, using a numerical example, we demonstrate that the incorporation of the PCM in a photonic structure can lead to a dramatic modification of the effects of light-induced phase transition, as compared to a stand-alone sample of the same PCM. Our focus is on short pulses. We discuss some possible applications of such phase-changing photonic structures for optical sensing and limiting.

DOI: 10.1103/PhysRevA.97.013804

I. INTRODUCTION

Phase-changing materials (PCMs) have been used in a variety of different applications in optics [1–6]. A typical optical PCM can be reversibly switched between two phases with different refractive index, optical absorption, or electrical conductance. The phase change can be caused by the input light itself (self-induced phase transitions) due to heating or some other physical mechanisms [7–9]. Alternatively, it can be induced by external heating or cooling, by application of an electric or magnetic field, or by mechanical stress [10–12]. In this paper, we exclusively focus on the effects of a self-induced phase transition in a phase-changing component of the photonic structure.

There are at least two different kinds of PCMs. An example of the first kind of PCMs is presented by germanium-antimony-tellurium alloys undergoing amorphous-to-crystalline phase transition when subjected to laser irradiation [13]. The two solid phases of this alloy have different refractive indices, but they are both stable at room temperature. The phase transition can be reversed by a laser pulse of different duration, or by the application of a dc electric field. This and similar systems revolutionized the media and data storage industries. A qualitatively different kind of optical PCM is presented by vanadium dioxide (VO_2) [14–16]. This material undergoes a dielectric-to-metal phase transition just above room temperature [17,18]. In this case, with the exception of a small hysteresis, only one of the two phases is stable at any given temperature. The dielectric phase is only stable below the phase transition temperature T_C, while the metallic phase is stable above T_C. The electric conductivity of the metallic phase is higher than that of the dielectric phase by 3–5 orders of magnitude [8,17,19–22]. The phase change from the dielectric to metallic state can be caused by light-induced heating. When the temperature drops below T_C, the dielectric phase is restored and the material returns to optical transparency. Optical PCMs of this second kind can be used in all-optical modulators, switches, IR sensors, and optical limiters. The focus of our study is on PCMs similar to VO_2, in which only one of the two phases can be stable at any given temperature. Since the two solid phases have different material properties, their optical characteristics will also be very different before and after the phase transition. This difference is the basis for all known practical applications of PCMs in optics.

In this study, we go further and investigate what happens if the PCM is not just a stand-alone (SA) layer, such as a film on a substrate, but a part of a multilayered photonic structure. A single PCM layer embedded in a photonic crystal would be the equivalent of a Fabry-Pérot étalon constructed with dielectric Bragg mirrors enclosing the PCM. More generally, we consider a PCM defect or a chain of PCM defects embedded in a photonic band-gap structure. Such structures, judiciously designed, can dramatically change the optical manifestation of the light-induced phase transition. Specifically, (1) it can qualitatively modify the transmission characteristics of the photonic structure associated with the phase transition in its phase-changing component; (2) it can significantly change, either increase or decrease, the critical value of the input light intensity triggering the phase transition; and (3) it can protect the PCM from the heat-related damage by shielding it from high-intensity input light after transition to the high-temperature phase has occurred. The above effects are strongly dependent on the pulse duration and the thickness of the PCM layer.

This paper presents the results of time-domain numerical simulations for the case of short input pulses with fluence large enough to trigger the dielectric-to-metal phase transition in the PCM. We compare the results for a stand-alone PCM layer with those for the same PCM layer incorporated in a layered structure. We show that a judiciously designed photonic structure can: (1) drastically reduce the critical value of the input light fluence (hereinafter, the input fluence threshold, IFT), triggering the onset of the dielectric-to-metal phase transition in the PCM; (2) reduce the transmittance above the input fluence threshold by orders of magnitude, while rendering the layered structure highly reflective; (3) significantly reduce the field intensity in the vicinity of the PCM layer above the input fluence threshold, thereby preventing the PCM layer from overheating; and (4) significantly enhance the field intensity in the vicinity of the defect layer below the input fluence

threshold. The first three features relate to high-fluence pulses; they can be particularly attractive for optical limiting and switching. The fourth feature can be useful for the resonant enhancement of sensor sensitivity [23].

As a numerical example, we consider a periodic layered structure with vanadium dioxide as a phase-changing defect layer. This simple arrangement allows us to illustrate all the features listed above. Although we choose the mid-infrared domain (specifically, 4-μm wavelength) where there is a rather large atmospheric transparency window, similar consideration can be applied to many other wavelengths.

We stress again that there are various existing proposals associated with intensity (or fluence) sensitive optical switches. For instance, a single VO_2 layer would act as an optical limiter or switch [24–27]. At the same time there are many other publications considering the switching properties of photonic structures with different types of optical nonlinearities, such as two-photon absorption (TPA) or nonlinear Kerr effects [28–35]. To our knowledge, the case of a phase-changing material being a part of photonic structure with engineered dispersion is yet to be considered. In this paper, we highlight the differences between a photonic structure with a PCM component (such as VO_2) versus (i) a stand-alone PCM layer and (ii) a photonic structure with a nonlinear component (see Conclusions).

The paper is organized as follows. In Sec. II we present the specifics of the photonic structure with phase-changing defect based on vanadium dioxide. In Sec. III we briefly present a semiqualitative study of the transport characteristics of an incident monochromatic field in the steady-state regime. However, our main focus is on numerical study of the case of short input pulses, as presented in Sec. IV. The modeling of the full transient electromagnetic pulse propagation coupled with heat-transfer analysis is presented in Sec. IV A, while the analysis of our simulations is presented in Sec. IV B. A generalization for the case of multiple defects is also considered and presented in Sec. V. The results are summarized in the final section, Sec. VI.

II. PHOTONIC CRYSTAL WITH PHASE-CHANGING DEFECTS

Consider an interference filter consisting of two alternating quarter-wavelength dielectric layers L and H having low and high refractive indices, respectively. A PCM defect layer D of half-wavelength thickness d is embedded at the mirror symmetry plane of the multilayered structure. In the more general case of multiple defects discussed in Sec. V, their positions will be appropriately chosen in a way that the total multilayered photonic structure will still respect a mirror symmetry. We shall refer to these generic embedded defects in the photonic structure as EDPS. Such a photonic structure has layering described by the sequence $(LH)^m D[(HL)^n HD]^{p-1}(HL)^m$, where $p = 1,2,\ldots$ corresponds to one, two, three, etc. defect layers. The integer m denotes the number of alternating bilayers LH located at each end of the structure, and n denotes the number of bilayers separating multiple defect layers. A schematic illustration of our proposed design for the case of a single defect (i.e., $p = 1$) embedded in a layered structure consisting of $m = 5$ bilayers is shown in Fig. 1.

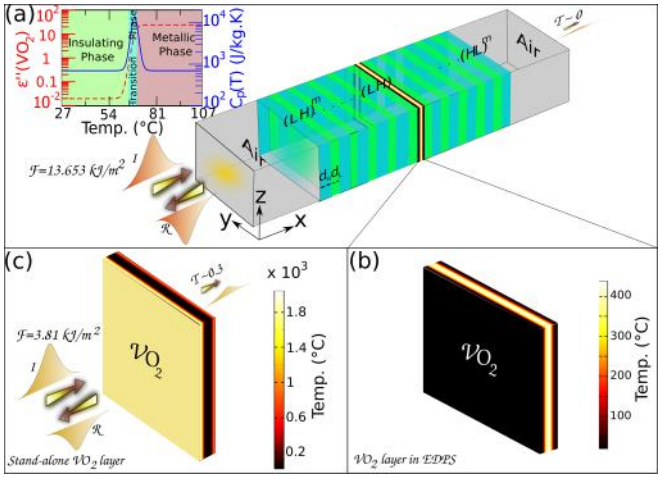

FIG. 1. (a) A schematic illustration of our proposed EDPS with a PCM defect layer. It consists of two alternating composite layers with low L (SiO_2) and high H (Si_3N_4) refractive indices and a defect (VO_2) layer placed at the plane of mirror symmetry of the structure. The two layers are quarter-wavelength thick while the defect layer is half-wavelength thick. Inset: The red dashed curve shows a typical behavior of $\epsilon''_D(T)$ using Eq. (1) with $\epsilon''_0 \approx 0.02$, $\Delta\epsilon''_D \approx 25$, and $\Delta \approx 1\,^\circ$C [36,37]. The solid blue curve shows the temperature variation of the specific heat C_P of the VO_2 layer due to the released latent heat during the dielectric-to-metal phase transition, see Eq. (2). (b) Magnified view of the thermal density distribution within the VO_2 layer in the EDPS for a high-intensity incident light with $\mathcal{F} = 13.653\,\frac{\text{kJ}}{\text{m}^2}$. (c) The thermal density distribution within the VO_2 layer in the SA layered structure for an input light with $\mathcal{F} = 3.81\,\frac{\text{kJ}}{\text{m}^2}$. In this case the SA already surpasses the melting point ($\sim$1967 °C) of the VO_2 layer.

In our simulations we use silicon dioxide (SiO_2) for the low-index layers L and silicon nitride (Si_3N_4) for the high-index layers H, with respective (real) permittivity values $\epsilon'_L = 1.9396$ and $\epsilon'_H = 5.7312$, respectively. We further assume that at the operational wavelength $\lambda_0 = 4\ \mu$m (midwave IR), these materials have negligible absorption, i.e., $\epsilon''_{L/H} \approx 0$. The VO_2 defect layer experiences its sharp dielectric-to-metal transition at around $T_C \approx 341$ K (68 °C) and has been studied extensively because of this near-room-temperature phase transition as well as its high phase stability. The high-temperature metallic phase to a low-temperature dielectric phase is accompanied by a structural phase transition from a rutile to a monoclinic structure. As a result, not only is there a dramatic change in its complex permittivity $\epsilon_D = \epsilon'_D + i\epsilon''_D$, but there is also a significant latent heat.

Although various experimental studies for VO_2 give different values of its permittivity in the dielectric and the metallic phase, all of them seem to agree that the changes in ϵ''_D can be as high as 4, or even 5 orders of magnitude in the midinfrared domain [4,8,14,17,38]. The variation in the exact values is mainly attributed to the fabrication process, preparation, and the quality of the VO_2 sample, and in the experimental techniques used to measure its permittivity. In our simulations, we are required to model this abrupt change in ϵ''_D near the phase transition temperature as a continuous transition. We use an exponentially broadened step function fit

to experimental data, expressed as

$$\epsilon_D''(T) = \epsilon_0'' + \left[\frac{\Delta\epsilon_D''}{\exp\left[-(T-T_C)/\Delta\right]+1}\right]. \quad (1)$$

The constants ϵ_0'' and $\Delta\epsilon_D''$ have been extracted from various experimental data presented in the literature in a way that matches the observed values of ϵ_D'' in the dielectric and metallic phase [4,14,39–41]. We have found that ϵ_0'' can take values between 0.02 (or even lower) to 0.1 while the extracted $\Delta\epsilon_D''$ varies between 25 and 80. In order to test the dependence of our conclusions on these variations, we have performed simulations using two sets of parameters $(\epsilon_0'', \Delta\epsilon_D'')$ corresponding to (0.1,25) (range I) and (0.02,25) (range II). The functional dependence of $\epsilon_D''(T)$ on temperature T is shown in the inset of Fig. 1 (dashed lines) for range II. In both cases the results for the transport characteristics of our structure remain qualitatively the same. The "smoothing" parameter Δ over which the transition occurs is taken to be $\Delta \approx 1$ K (see Sec. IV). Nevertheless, we have checked that values of Δ of up to 4 K show the same qualitative picture for the transmission properties of our structures. Finally, for simplicity we assume that the real part of permittivity remains approximately constant, and take $\epsilon_D' = 8.41$ [42].

Another thermal parameter that arises from the dielectric-to-metal transition is the specific heat capacity C_p^D at constant pressure of the VO_2 layer. In our continuous model, the latent heat of transition, which has been measured to be $H_L \approx 5.042 \times 10^4$ J/kg [43,44], is distributed through the transition as an additional temperature-dependent specific heat term on top of a relatively constant background, $C_p^{(0)} \approx 700\ \mathrm{J\,kg^{-1}\,K^{-1}}$. This additional term is taken to be proportional to the extent of the conductivity change so that

$$C_p^D(T) = C_p^{(0)} + \frac{H_L}{\Delta\sigma_t}\frac{d\sigma}{dT}, \quad (2)$$

where $\Delta\sigma_t \approx 9.96 \times 10^4$ (S/m) is the total conductivity jump during the phase transition, consistent with $\epsilon_D''(T)$ of Eq. (1). This model dependence of $C_p^D(T)$ Eq. (2) on temperature for $\Delta = 1$ K is also shown in the inset of Fig. 1 with a blue solid line. Finally, in our calculations below we have also considered the changes in thermal conductivity k_D occurring during the phase transition. Specifically, we have assumed that $k_D = 4\frac{\mathrm{W}}{\mathrm{mK}}$ in the dielectric phase below T_c, changing to $k_D = 6\frac{\mathrm{W}}{\mathrm{mK}}$ in the metallic phase [45].

III. FREQUENCY DOMAIN ANALYSIS

Let us start with the semiqualitative frequency domain analysis of steady-state regime. It will provide us with the understanding of what to expect from the time-domain simulations for the case of short pulses presented in the next section.

The electric component of a time-harmonic monochromatic field satisfies the Helmholtz equation

$$\nabla^2\vec{E}(x) + k^2\epsilon(x)\vec{E}(x) = 0, \quad (3)$$

where $k = 2\pi\nu/c$ is the wave number, $\epsilon(x)$ is the spatially varying permittivity of the structure along the propagation direction x, c is the speed of light in the vacuum, and ν is its frequency (Hz). The scattering fields, and therefore

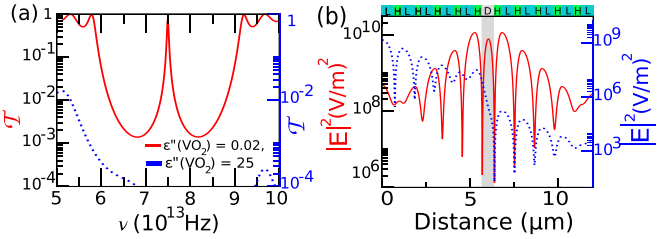

FIG. 2. (a) Transmission spectra obtained for the single VO_2 layer in our EDPS of Fig. 1. The solid red curve corresponds to $\epsilon_D'' = 0.02$ (dielectric phase), and the dotted blue curve corresponds to $\epsilon_D'' = 25$ (metallic phase) [range II associated with Eq. (1)]. (b) The spatial electric field intensity distribution at the resonant frequency, $\nu_0 = 7.5 \times 10^{13}$ Hz, associated with the defect mode of the EDPS [styles as in (a)]. For a low incident fluence (i.e., $\epsilon_D'' \approx \epsilon_0'' = 0.02$) the structure supports a resonant mode which is exponentially localized within the defect layer (solid red curve). When the incident signal has a large fluence, the VO_2 layer is heated up and its imaginary permittivity increases dramatically, i.e., $\epsilon_D''= 25$ (see inset of Fig. 1). In this case the defect resonant mode is destroyed and the electric field intensity at the position of the defect layer decreases exponentially from its incident value (dotted blue curve). The position of the L (SiO_2) and H (Si_3N_4) layers and the position of the defect layer (gray) are indicated as bars at the upper axis of the figure.

the frequency-dependent transmittance $\mathcal{T}$, reflectance $\mathcal{R}$, and absorptance $\mathcal{A}$, have been calculated numerically from Eq. (3) using the standard transfer matrix approach [46,47].

The frequency-dependent transmittance $\mathcal{T}(\nu)$, reflectance $\mathcal{R}(\nu)$, and absorptance $\mathcal{A}(\nu)$ are defined as

$$\mathcal{T}(\nu) = \frac{S_{\mathrm{tr}}(\nu)}{S_{\mathrm{in}}(\nu)},\ \mathcal{R}(\nu) = \frac{S_{\mathrm{refl}}(\nu)}{S_{\mathrm{in}}(\nu)},\ \mathcal{A}(\nu) = 1-\mathcal{T}(\nu)-\mathcal{R}(\nu), \quad (4)$$

where $S(\nu) = \frac{1}{2}\mathcal{R}e(EH^*)$ is the real-valued energy flux normal to the outer air boundaries. Using Eqs. (3) and (4), we can calculate the transmission spectrum for the case of one $p = 1$ defect embedded in an interference filter (i.e., photonic crystal) with $m = 5$ bilayers.

At low light intensity, the heating of the VO_2 layer is negligible, and thus its temperature T remains below the critical phase transition temperature value T_C. In this case, the VO_2 defect layer is in the dielectric state with the low value of ϵ_0''. The low-intensity transmittance as a function of frequency is shown in Fig. 2(a) in solid red. The resonant transmission peak in the figure corresponds to the frequency of the localized defect mode. The resonant mode profile is shown in Fig. 2(b), also in solid red. If the light intensity is high enough, the VO_2 layer is heated above T_C. In this case, the VO_2 defect layer is in the metallic state indicated by the large value of ϵ_D''. The latter results in suppression of the localized mode, along with the resonant transmission, as seen in Figs. 2(a) and 2(b) (see the dotted blue lines). The transmission peaks at the pass band (associated with the Fabry-Pérot resonances of the structure) are also suppressed, see Fig. 2(a), due to the increase of the absorption from the PCM layer. The latter is associated with the abrupt increase of ϵ_D'' at the metal phase.

Let us now turn our attention to the transport properties of the resonant defect mode which is the focus of this paper. A

simple way to explain the destruction of the resonant transmission via the defect mode is by realizing that its existence is a result of two competing dissipation mechanisms. The first one is the effect of losses due to radiation from the boundaries of the layered structure. An estimate of its magnitude is given by the linewidth Γ_R of the associated resonant mode. The second one is due to the ohmic loss Γ_{Ohm} occurring in the high-temperature (metallic) phase of VO_2. One can estimate these losses to be

$$\Gamma_R \approx \frac{1}{\xi}\exp(-2L/\xi), \quad \Gamma_{Ohm} \approx k\epsilon_D'' \frac{d}{\xi}, \tag{5}$$

where L in Eq. (5) is the total thickness of the layered structure, d is the width of the defect layer, and ξ is the so-called localization length of the defect mode. The latter is proportional to the inverse of the decay rate of the resonant defect mode intensity. [See red field intensity profile in Fig. 2(b).] In the *underdamping* limit $\Gamma_R \gg \Gamma_{Ohm}$, photons can transmit via the high-Q resonant defect mode through the layered structure, thus leading to high transmittance, i.e., $\mathcal{T}(\nu_r) \approx 1$. In this limit both reflection and absorption are vanishing i.e., $\mathcal{R}(\nu_r) \approx 0, \mathcal{A}(\nu_r) \approx 0$. As ϵ_D'' increases, the absorption coefficient $\mathcal{A}$ increases initially linearly and reaches a maximum value at some $\epsilon_D''^{CC}$ with a simultaneous decrease (increase) in $\mathcal{T}$ ($\mathcal{R}$) (CC denotes the critical coupling). The maximum absorption occurs when *critical coupling* is achieved, i.e., when ohmic and radiative losses are optimally balanced. In the domain $\epsilon_D'' < \epsilon_D''^{CC}$ the dominant dissipation mechanism is still associated with radiative losses and the incident photons spend enough time in the resonant mode in order to be eventually absorbed, thus increasing the ohmic losses at the VO_2 layer. A further increase in ϵ_D'' leads to a noticeable decrease in $\mathcal{A}$ and a simultaneous increase (decrease) in reflection (transmittance). This is the *overdamping* limit $\Gamma_R \ll \Gamma_{Ohm}$, where the dominant dissipation mechanism is associated with the ohmic losses. The associated dwell time is $\tau_{dwell}^{-1} \approx \Gamma_{Ohm}$; thus the incident photons do not dwell for long enough time inside the cavity in order to be absorbed by the VO_2 layer. Rather, they are reflected back to space, thus increasing the reflectance of the photonic structure. For even larger values of ϵ_D'', a complete destruction of the resonant mode takes place and the entire energy is reflected, i.e., $\mathcal{R} \approx 1$ while the absorbed energy is essentially zero $\mathcal{A} \approx 0$. In simple terms, the VO_2 defect, being in the metallic phase, has completely decoupled the left and right parts of the photonic structure, which now acts as an (almost) perfect mirror.

IV. SHORT PULSES

We now turn to the study of the transport characteristics of the layered structure of Fig. 1 in the case of short-pulse incident beams. In Sec. IV A we present the mathematical model that describes the propagation of a beam in the presence of a temperature-varied defect permittivity. The results of the time-domain simulations and the conclusions about the transport characteristics of the layered structure, in the case of short incident pulses, is presented in the subsequent section, Sec. IV B.

A. Time-domain electromagnetic and heat-transfer model setup

The pulse propagation in the case of temperature-varying permittivity of the VO_2 layer is described by the following set of coupled electromagnetic and thermal equations:

$$\nabla \times \vec{H} = \vec{J} + \epsilon'(x)\frac{\partial \vec{E}}{\partial t}, \quad \nabla \times \vec{E} = -\mu(x)\frac{\partial \vec{H}}{\partial t}, \tag{6a}$$

$$\rho_D C_p^D \frac{\partial T}{\partial t} - \nabla \cdot (k_D \nabla T) = Q, \quad Q = \vec{J} \cdot \vec{E}, \tag{6b}$$

where $\mu(x) = \mu_0$ is the permeability of the composite materials, and $\vec{J} = \sigma(T)\vec{E}$ is the current density. The thermal conductivity of the VO_2 layer is k_D, C_p^D is the specific heat capacity at constant pressure, and $\sigma(T)$ is the electrical conductivity described earlier and shown in the inset of Fig. 1. In the above coupled electromagnetic-heat-transfer model, the absorbed power Q deposited per unit volume within the defect layer(s) from the incident electromagnetic pulse leads to an increase of temperature T within the VO_2 layer as described by the rate equation (6b). Finally, ρ_D corresponds to the mass density of the VO_2 layer. Maxwell's equations (6a) are solved together with the conductive heat-transfer equation (6b) using commercially available COMSOL MULTIPHYSICS software [48].

In all our simulations we consider Gaussian modulated incident pulses with a carrier frequency of $\nu_0 \approx 7.5 \times 10^{13}$ Hz (free wavelength $\lambda_0 = 4\ \mu$m), corresponding to the defect resonant mode supported by the layered structure of Fig. 1 [shown in the transmission spectra in Fig. 2(a)]. The associated time-varying electric field $E(t)$ of the incident pulse is

$$E(t) = E_0 \exp[-0.5(t/\tau)^2]\cos(k_0 x - 2\pi\nu_0 t), \tag{7}$$

where E_0, t, τ, and k_0 denotes the peak electric field amplitude, time, width, and wave number ($2\pi/\lambda_0$) of the input signal, respectively.

The pulse width τ was always chosen long enough to assure a spectrum consistent with the bandwidth of the midgap transmission peak of Fig. 2(a), thus assuring maximum transmittance for low fluence. The accuracy of the time integrations was checked by decreasing the time-step by half to confirm that the results of the simulations remain unchanged.

Generally, both τ or E_0 could be increased with equivalent results, with the fluence evaluated as $\mathcal{F} = (\sqrt{\pi}/2)c\epsilon_0 E_0^2 \tau$. In our simulations the pulse width τ was limited to less than 0.5 ns due to numerical integration constraints, and we limited the electric field to within reasonable breakdown strengths. Nevertheless, one can extrapolate the validity of our results for pulse durations as large as the thermal relaxation time $\tau_D \approx l^2/D \approx 10$ ns, where $D = k_D/\rho_D C_p$ is the thermal diffusion constant and $l \approx 0.13\ \mu$m is the thermal relaxation length. The latter was estimated from our simulations by evaluating the FWHM of the temperature profile inside the VO_2 layer when it reaches its maximum value (i.e., for $\mathcal{F} = 13.653$ kJ/m^2).

Using the above calculation scheme we evaluated the total $\mathcal{T}$, $\mathcal{R}$, and $\mathcal{A}$ numerically using the expressions

$$\mathcal{T} = \frac{\int_0^\infty \bar{P}_{tr}(t)dt}{\int_0^\infty \bar{P}_{in}(t)dt}, \quad \mathcal{R} = \frac{\int_0^\infty \bar{P}_{refl}(t)dt}{\int_0^\infty \bar{P}_{in}(t)dt}, \quad \mathcal{A} = 1 - \mathcal{T} - \mathcal{R}, \tag{8}$$

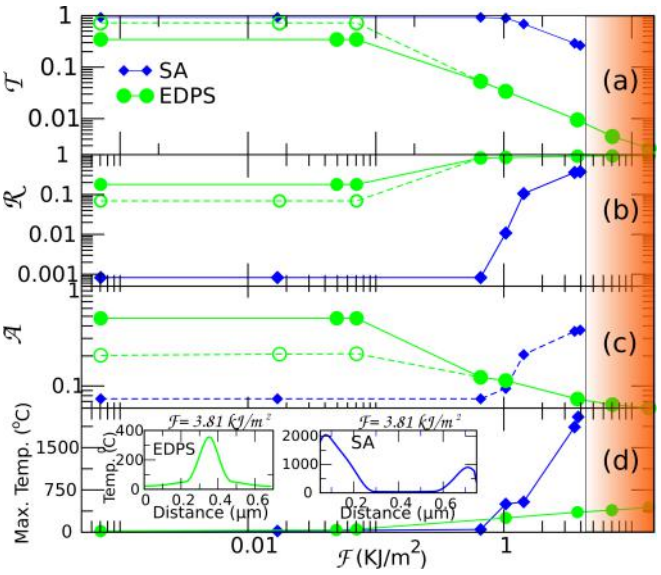

FIG. 3. The time-cumulative (a) transmittance ($\mathcal{T}$), (b) reflectance ($\mathcal{R}$), and (c) absorptance ($\mathcal{A}$) versus the fluence $\mathcal{F}$ of an incident pulse. We consider the case of the VO_2 layer in the EDPS of Fig. 1, represented by the circle curves. The EDPS demonstrates high transmittance for pulses with lower fluence while it becomes completely reflective for pulses with high fluence. The filled circles correspond to parameters $\epsilon_0'' \approx 0.1$, $\Delta\epsilon_D'' = 25$, $\Delta = 1\,^\circ$C (range I), while the empty circles to $\epsilon_0'' \approx 0.02$, $\Delta\epsilon_D'' = 25$, $\Delta = 1\,^\circ$C (range II). The transmission characteristics of the multilayered structure is compared with that of a stand-alone VO_2 structure represented by the blue filled diamonds, where a significant absorption occurs for high-fluence pulses. In (d) we report the maximum temperature reached within the VO_2 layer for incident pulses with various fluence $\mathcal{F}$. The insets show the spatial temperature profiles inside the VO_2 layer for the EDPS and SA configurations. The highlighted orange area indicates the fluence regime for which the SA VO_2 layer has reached temperatures higher than its melting temperature $T \approx 1967\,^\circ$C.

where $\bar{P}_j(t)$ is the energy power flowing across the incident ($j =$ in, refl) and exit surfaces (tr) of the structure.

B. Simulation result and discussion

A summary of our time-domain simulations for $\mathcal{T}$,$\mathcal{R}$, and $\mathcal{A}$ of Eq. (8) versus fluence for the case of a single VO_2 defect layer is shown in Figs. 3(a)–3(c), with the green circles corresponding to the embedded defect and the blue diamonds corresponding to the stand-alone layer. The filled and open circles correspond to range I and range II, respectively, for the different values of ϵ_0'' discussed in Sec. II [39,41]. Figure 3(d) shows the maximum temperature (in °C) reached inside the VO_2 layer during the simulations for the same fluence. The insets of Fig. 3(d) show typical spatial temperature profiles across the defect layer for times at the end of the simulation pulse.

We first note that in the case of the stand-alone defect layer the temperature profile reaches its maximum value near the boundary interfaces. In contrast, for the EDPS the maximum temperature is reached at the center of the defect where the electric field experiences its maximum value [see Fig. 2(b)].

We now discuss in more detail the transport features of the layered structure. Incident pulses with fluence $\mathcal{F} < 0.07$ kJ/m^2 do not cause any significant heating [see Fig. 3(d)] of the defect layer, resulting in a negligible increase in $\epsilon_D''(T)$. In this case the resonant defect mode remains unaffected (see discussion in Sec. III) and dictates the transport characteristics of the incident pulse. Specifically, we find that the transmittance can be larger than 35%–40% for VO_2 films with $\epsilon_0'' \approx 0.1$ (range I) in the dielectric phase (see filled symbols in Fig. 3). For $\epsilon_0'' \approx 0.02$ (range II) the transmittance can reach values as high as 75% (see open symbols in Fig. 3).

As the fluence of the pulse increases beyond $\mathcal{F} \geqslant 0.07$ kJ/m^2, the induced heating effects become important. Specifically, the temperature at the VO_2 layer rises above T_C, driving the defect layer into the metallic phase. In all our simulations we have found that the time duration for which the permittivity $\epsilon_D''(T > T_C)$ changes significantly is typically less than 0.01 ps. At this point the resonant defect mode has been completely suppressed [see Figs. 2(a) and 2(b)], leading to a sharp decrease in transmittance [see Fig. 3(a)]. In contrast, the transmission of the VO_2 SA layer is still $\mathcal{T} \approx 1$ for fluence as high as $\mathcal{F} \approx 1$ kJ/m^2. The simulations of Fig. 3(a) indicate that the input fluence threshold, $\mathcal{F}_{\rm IFT}$, of our layered structure can be at least 1 order of magnitude smaller than the input fluence threshold provided by the stand-alone VO_2 layer. The low value of $\mathcal{F}_{\rm IFT}$ of the layered structure is another consequence of the exponential sensitivity of the transition to the overdamping regime enabled by the nature of the resonant defect mode [see Eq. (5) and relevant discussion]. The underdamping-to-overdamping transition is also responsible for the increase in reflectance, which for fluences $\mathcal{F} \geqslant 1$ kJ/m^2 is approximately 100%. At the same time the absorptance $\mathcal{A}$ decays to zero (see discussion in Sec. III). Again, contrast this behavior with the stand-alone VO_2 layer, which has already reached temperatures above the melting point $T_{\rm melt} \approx 1967\,^\circ$C for fluences $\mathcal{F} \approx 4$ kJ/m^2 [see Fig. 3(d)] [49]. We therefore conclude that the EDPS design provides protection from overheating of the VO_2 layer and thus prevents its destruction from high-fluence incident radiation.

The EDPS of Fig. 1(a) can be utilized as a photonic limiter. These are devices that protect sensitive sensors by blocking high-fluence (or power) incident radiation while transmitting low-level radiation. Many of the existing limiters achieve this goal by absorbing most of the incident pulse energy, an operation that leads to their overheating and destruction (sacrificial limiters), exemplified by the stand-alone VO_2 layer. Instead, the layered structure of Fig. 1(a) has an improved *damaged threshold* (DT) since it reflects the harmful high-fluence radiation back to space. At the same time it demonstrates a low $\mathcal{F}_{\rm IFT}$, which is considered another important feature of an efficient photonic limiter. It is usually referred to as the *limiting threshold* of the limiter and should always be well below the damage threshold of the sensor that the limiter is protecting. The ratio between the limiter's own damage threshold and limiting threshold $\mathcal{F}_{\rm IFT}$ provides the figure of merit of the limiter, also referred to as its *dynamical range*. Our numerical simulations clearly demonstrate that the embedded limiter has increased its dynamic range by at least 2 orders of magnitude as compared to the single layer.

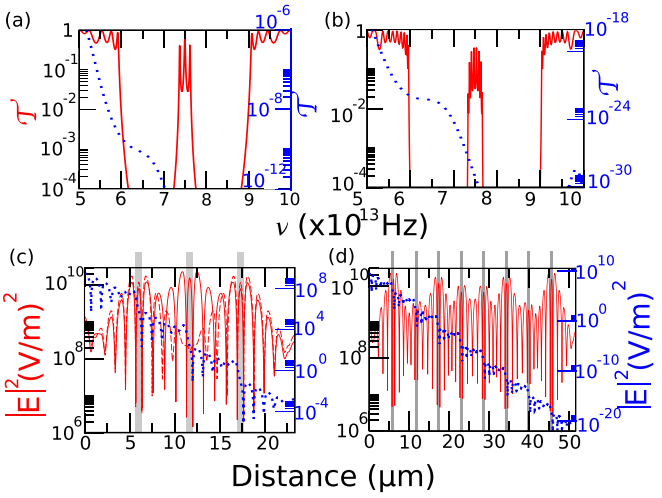

FIG. 4. Transmission spectra obtained for the layered structure incorporating (a) three VO_2 defects and (b) eight VO_2 defects. The defects are placed in a way that the whole structure respects a mirror symmetry. Two scenarios corresponding to $\epsilon''_D = 0.02$ (dielectric phase) and 25 (metallic phase) of the VO_2 layer are depicted with solid red and dotted blue lines, respectively. The spatial electric field intensity distributions of the resonant mode for the case of the EDPS incorporating (c) three VO_2 defects and (d) eight VO_2 defects are shown, respectively. The red dash and solid lines in (c) denote the symmetric and asymmetric mode profiles at the resonant frequencies of 7.373×10^{13} Hz and 7.495×10^{13} Hz for the case when $\epsilon''_D = 0.02$. The gray vertical bars denote the position of the defect layers within the layered photonic structure.

V. GENERALIZATION TO MULTIPLE DEFECTS

Next we generalize the above study for the case of multiple VO_2 defects. The transmission spectra for three ($p = 3$) and eight ($p = 8$) defects are reported in Figs. 4(a) and 4(b), while the profiles of the associated defect modes are shown in Figs. 4(c) and 4(d). These calculations have been done for low light intensities (solid red lines) and high light intensities (dotted blue lines using range I, see Sec. II). The new element in these multidefect configurations, as opposed to the one-defect case of Fig. 2, is the appearance of other resonant modes in the vicinity of the center of the band gap which leads to the creation of a miniband [see solid red lines in Figs. 4(a) and 4(b)].

We understand the formation of the miniband as follows. Consider identical single-defect layered structures. From the discussion at Sec. III we know that each of these configurations can support a defect mode which is exponentially localized around the defect. When these identical singe-defect layered structures are brought together at some finite distance L_d from one another (i.e., when the portion of the layered structure which is surrounding the defects becomes finite), the defect mode associated with each configuration can be evanescently coupled with its degenerate pair supported by the nearby configuration. The coupling constant between them is $q \approx \exp(-L_d/\xi)$. This coupling lifts the degeneracy and leads to the creation of the minibands within the band gap of the combined layered structure, having bandwidth proportional to q. The associated states are symmetric and antisymmetric linear combinations of the single defect modes, and their profiles have a multihumped shape, with each hump located in the neighborhood of a defect [see Figs. 4(c) and 4(d) for a three- and an eight-defect-mode configuration]. The above picture is valid as long as the total losses (i.e., the sum of the radiative losses due to leakage and the ohmic losses due to small ϵ''_D at the defects) are much smaller than the coupling q. This requirement is satisfied as long as the incident field carries a small fluence, so that the VO_2 defects are in the dielectric phase where $\epsilon''_D \approx \epsilon''_0 \approx 0$. Similar to the one-defect case, in this limit the transport is dictated by the presence of multihump mirror symmetric states which lead to high transmittance $\mathcal{T} \approx 1$ [see red solid lines in Figs. 4(a) and 4(b)].

Once the incident fluence increases, the temperature at the defect layers increases above the dielectric-to-metal transition temperature T_C. The ohmic dissipation at the VO_2 layers increases dramatically, and the total losses become larger than the coupling q. In this case the same scenario as in the case of one defect applies, namely, the multihumped modes are destroyed [see blue lines in Figs. 4(c) and 4(d)], leading to a suppression of transmittance $\mathcal{T} \approx 0$ [blue lines in Figs. 4(a) and 4(b)] and a consequent increase (decrease) of reflectance (absorptance), i.e., $\mathcal{R} \approx 1$ and $\mathcal{A} \approx 0$, respectively.

In Figs. 5(a)–5(c) we report the transport characteristics of our layered structure for the case of short incident pulses for $p = 3$. In this case the advantage of the miniband formation is

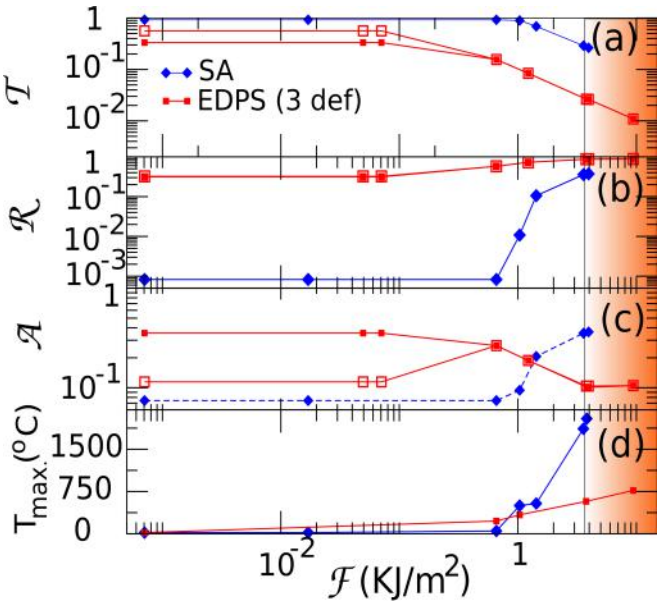

FIG. 5. Time-cumulative (a) transmittance $\mathcal{T}$, (b) reflectance $\mathcal{R}$, and (c) absorptance $\mathcal{A}$ versus the fluence $\mathcal{F}$ for the case of three ($p = 3$) VO_2 defects embedded within our proposed multilayered structure. The result is compared with that obtained for the SA layered structure shown by the blue diamond curve. (d) The maximum temperature reached inside the VO_2 layer during the simulation period for varying fluences of the incident pulse. The orange highlighted domain corresponds to fluences for which the SA VO_2 layer has already reached its melting temperature of 1967 °C. In all the subfigures filled symbols indicate simulations with permittivity parameters associated with range I while open symbols indicate simulations with permittivity parameters associated with range II.

translated to a tolerance in choosing a central pulse frequency anywhere inside the miniband, i.e., $\nu_0 \pm q$ and, nevertheless, have high transmittance at low fluences. At the same time these pulses will be (almost) completely reflected when their fluence is high enough. The underlying mechanism is the same as the one found for the case of a layered structure with a single VO_2 defect (see previous section) and it is associated with the light-induced phase transition of the VO_2 layer and its modifications in the presence of a layered structure.

VI. CONCLUSION

In summary, let us highlight the most important features of the transmission properties of the planar resonant cavity in Fig. 1 containing a PCM represented by VO_2. If the input pulse duration is much greater than the thermal relaxation time of the PCM layer, the layered structure acts as a reflective irradiance limiter described in [50]. Specifically, the transition from the resonance transmission to high reflectance associated with the dielectric-to-metal phase transition occurs at much lower input light intensity compared to the same PCM layer taken out from the photonic resonant cavity (i.e., for a SA layered structure). After the phase transition is completed, the field intensity at the PCM layer becomes much lower than that of the incident light, and the entire structure becomes highly reflective, which prevents it from overheating. If the pulse duration is much shorter than the thermal relaxation time of the PCM layer, the structure acts as a reflective fluence limiter described in [51]. Yet, there is a big difference between the approach [50–52] based on optical materials with nonlinear absorption incorporated into a photonic structure and the current approach based on a PCM. In the former case, the transition from high transmittance to high reflectance may require orders-of-magnitude change in the input light intensity. By contrast, a judiciously designed photonic structure incorporating a PCM can provide an abrupt transition from nearly perfect transmittance to nearly perfect reflectance at a desired irradiance or fluence. In either case, using a chain of coupled defect layers instead of a single one alleviates the bandwidth restrictions and ensures enhanced performance even for very short input pulses.

ACKNOWLEDGMENTS

The authors would like to thank Dr. M. Kats for many useful discussions on phase-change materials. We acknowledge support from the ONR via Grant No. N00014-16-1-2803 (R.T. and T.K.), from the AFOSR via Grant No. LRIR14RY14COR (I.V.), and from the NSF via Grant No. DMR-1306984 (F.M.E).

[1] S. Moller, C. Perlov, W. Jackson, C. Taussig, and S. R. Forrest, A polymer/semiconductor write-once read-many-times memory, Nature (London) **426**, 161 (2003).

[2] T. Rueckes, K. Kim, E. Joselevich, G. Y. Tseng, C.-L. Cheung, and C. M. Lieber, Carbon nanotube-based nonvolatile random access memory for molecular computing, Science **289**, 94 (2000).

[3] Q. H. Wang, K. Kalantar-Zadeh, A. Kis, J. N. Coleman, and M. S. Strano, Electronics and optoelectronics of two-dimensional transition metal dichalcogenides, Nat. Nanotechnol. **7**, 699 (2012).

[4] M. M. Qazilbash, M. Brehm, B.-G. Chae, P.-C. Ho, G. O. Andreev, B.-J. Kim, S. J. Yun, A. V. Balatsky, M. B. Maple, F. Keilmann, H.-T. Kim, and D. N. Basov, Mott transition in VO_2 revealed by infrared spectroscopy and nano-imaging, Science **318**, 1750 (2007).

[5] Q. Wang, E. T. F. Rogers, B. Gholipour, C. M. Wang, G. Yuan, J. Teng, and N. I. Zheludev, Optically reconfigurable metasurfaces and photonic devices based on phase change materials, Nat. Photonics **10**, 60 (2015).

[6] J. You, L. Meng, T.-B. Song, T.-F. Guo, Y. Yang, W.-H. Chang, Z. Hong, H. Chen, H. Zhou, Q. Chen, Y. Liu, N. De Marco, and Y. Yang, Improved air stability of perovskite solar cells via solution-processed metal oxide transport layers, Nat. Nanotechnol. **11**, 75 (2016).

[7] D. Fausti, R. I. Tobey, N. Dean, S. Kaiser, A. Dienst, M. C. Hoffmann, S. Pyon, T. Takayama, H. Takagi, and A. Cavalleri, Light-induced superconductivity in a stripe-ordered cuprate, Science **331**, 189 (2011).

[8] F. J. Morin, Oxides Which Show a Metal-to-Insulator Transition at the Neel Temperature, Phys. Rev. Lett. **3**, 34 (1959).

[9] D. N. Basov, R. D. Averitt, D. V. Marel, M. Dressel, and K. Haule, Electrodynamics of correlated electron materials, Rev. Mod. Phys. **83**, 471 (2011).

[10] T. Peterseim, T. Ivek, D. Schweitzer, and M. Dressel, Electrically induced phase transition in α-(BEDT-TTF)$_2$I$_3$: Indication for Dirac-like hot charge carriers, Phys. Rev. B **93**, 245133 (2016).

[11] M. Xua, Y. Q. Chenga, L. Wang, H. W. Shenge, Y. Meng, W. G. Yang, X. D. Hang, and E. Maa, Pressure tunes electrical resistivity by four orders of magnitude in amorphous $Ge_2Sb_2Te_5$ phase-change memory alloy, PNAS **109**, E1055 (2011).

[12] J. Locquet, J. Perret, and J. Fompeyrine, Doubling the critical temperature of $La_{1.9}Sr_{0.1}CuO_4$ using epitaxial strain, Nature (London) **394**, 453 (1998).

[13] I. Friedrich, V. Weidenhof, W. Njoroge, P. Franz, and M. Wuttig, Structural transformations of $Ge_2Sb_2Te_5$ films studied by electrical resistance measurements, J. Appl. Phys. **87**, 4130 (2000).

[14] M. A. Kats, R. Blanchard, P. Genevet, Z. Yang, M. M. Qazilbash, D. N. Basov, S. Ramanathan, and F. Capasso, Thermal tuning of mid-infrared plasmonic antenna arrays using a phase change material, Opt. Lett. **38**, 368 (2013).

[15] M. Liu, A. J. Sternbach, M. Wagner, T. V. Slusar, T. Kong, S. L. Bud'ko, S. Kittiwatanakul, M. M. Qazilbash, A. McLeod, Z. Fei, E. Abreu, J. Zhang, M. Goldflam, S. Dai, G.-X. Ni, J. Lu, H. A. Bechtel, M. C. Martin, M. B. Raschke, *et al.*, Phase transition in bulk single crystals and thin films of VO_2 by nanoscale infrared spectroscopy and imaging, Phys. Rev. B **91**, 245155 (2015).

[16] J. B. Goodenough, Anomalous Properties of the Vanadium Oxides, Annu. Rev. Mater. Sci. **1**, 101 (1971).

[17] M. Liu, H. Y. Hwang, H. Tao, A. C. Strikwerda, K. Fan, G. R. Keiser, A. J. Sternbach, K. G. West, S. Kittiwatanakul, J.

Lu, S. A. Wolf, F. G. Omenetto, X. Zhang, K. A. Nelson, and R. D. Averitt, Terahertz-field-induced insulator-to-metal transition in vanadium dioxide metamaterial, Nature (London) **487**, 345 (2012).

[18] C. Kubler, H. Ehrke, R. Huber, R. Lopez, A. Halabica, R. F. Haglund, and A. Leitenstorfer, Coherent Structural Dynamics and Electronic Correlations During an Ultrafast Insulator-to-Metal Phase Transition in VO_2, Phys. Rev. Lett. **99**, 116401 (2007).

[19] M. Kats, D. Sharma, J. Lin, P. Genevet, R. Blanchard, Z. Yang, M. M. Qazilbash, D. N. Basov, S. Ramanathan, and F. Capasso, Ultra-thin perfect absorber employing a tunable phase change material, Appl. Phys. Lett. **101**, 221101 (2012).

[20] M. R. M. Hashemi, C. W. Berry, E. Merced, N. Sepulveda, and M. Jarrahi, Direct measurement of vanadium dioxide dielectric properties in W-band, J. Infrared, Millimeter, Terahertz Waves **35**, 486 (2014).

[21] D. Fu, K. Liu, T. Tao, K. Lo, C. Cheng, B. Liu, R. Zhang, H. A. Bechtel, and J. Wu, Comprehensive study of the metal-insulator transition in pulsed laser deposited epitaxial VO_2 thin films, J. Appl. Phys. **113**, 043707 (2013).

[22] D. H. Kim and H. S. Kwok, Pulsed laser deposition of VO_2 thin films, Appl. Phys. Lett. **65**, 3188 (1994).

[23] T. Maier and H. Brueckl, Multispectral microbolometers for the midinfrared, Opt. Lett. **35**, 3766 (2010).

[24] S. Chen, H. Ma, X. Yi, H. Wang, X. Tao, M. Chen, X. Li, and C. Ke, Optical switch based on vanadium dioxide thin films, Infrared Phys. Tech. **45**, 239 (2004).

[25] M. Soltani, M. Chaker, E. Haddad, R. V. Kruzelecky, and D. Nikanpour, Optical switching of vanadium dioxide thin films deposited by reactive pulsed laser deposition, J. Vac. Sci. Technol. A **22**, 859 (2004).

[26] E. E. Chain, Optical properties of vanadium dioxide and vanadium pentoxide thin films, Appl. Opt. **30**, 2782 (1991).

[27] H. Wang, Y. Xinjian, S. Chen, and F. Xiaochao, Fabrication of vanadium oxide micro-optical switches, Sensors Act. A **122**, 108 (2005).

[28] A. Hache and M. Bourgeois, Ultrafast all-optical switching in a silicon-based photonic crystal, Appl. Phys. Lett. **77**, 4089 (2000).

[29] S. W. Leonard, H. M. van Driel, J. Schilling, and R. B. Wehrspohn, Ultrafast band-edge tuning of a two-dimensional silicon photonic crystal via free-carrier injection, Phys. Rev. B **66**, 161102(R) (2002).

[30] P. M. Johnson, A. F. Koenderink, and W. L. Vos, Ultrafast switching of photonic density of states in photonic crystals, Phys. Rev. B **66**, 081102(R) (2002).

[31] T. F. Boggess, S. C. Moss, I. W. Boyd, and A. L. Smirl, Nonlinear-optical energy regulation by nonlinear refraction and absorption in silicon, Opt. Lett. **9**, 291 (1984).

[32] J. H. Bechtel and W. L. Smith, Two-photon absorption in semiconductors with picosecond laser pulses, Phys. Rev. B **13**, 3515 (1976).

[33] M. Scalora, J. P. Dowling, C. M. Bowden, and M. J. Bloemer, Optical Limiting and Switching of Ultrashort Pulses in Nonlinear Photonic Band Gap Materials, Phys. Rev. Lett. **73**, 1368 (1994).

[34] X. Liu, J. W. Haus, and M. S. Shahriar, Optical limiting in a periodic materials with relaxational nonlinearity, Opt. Express **17**, 2696 (2009).

[35] M. Larciprete, C. Sibilia, S. Paoloni, M. Bertolotti, F. Sarto, and M. Scalora, Accessing the optical limiting properties of metallo-dielectric photonic band gap structures, J. Appl. Phys. **93**, 5013 (2003).

[36] J. Yoon, H. Kim, X. Chen, N. Tamura, B. S. Mun, C. Park, and H. Ju, Controlling the temperature and speed of the phase transition of VO_2 microcrystals, ACS Appl. Mater. Interfaces **8**, 2280 (2016).

[37] X. Xua, X. Hea, H. Wanga, Q. Gua, S. Shi, H. Xinga, C. Wanga, J. Zhanga, X. Chen, and J. Chu, The extremely narrow hysteresis width of phase transition in nanocrystalline VO_2 thin films with the flake grain structures, Appl. Surf. Sci. **261**, 83 (2012).

[38] H. W. Verleur, A. S. Barker, and C. N. Berglund, Optical Properties of VO_2 between 0.25 and 5 eV, Phys. Rev. **172**, 788 (1968).

[39] M. J. Dicken, K. Aydin, I. M. Pryce, L. A. Sweatlock, E. M. Boyd, S. Walavalkar, J. Ma, and H. A. Atwater, Frequency tunable near-infrared metamaterials based on VO_2 phase transition, Opt. Express **17**, 18330 (2009).

[40] T. Peterseim, M. Dressel, M. Dietrich, and A. Polity, Optical properties of VO_2 films at the phase transition: Influence of substrate and electronic correlations, J. Appl. Phys. **120**, 075102 (2016).

[41] J. B. K. Kana, J. M. Ndjaka, G. Vignaud, A. Gibaud, and M. Maaza, Thermally tunable optical constants of vanadium dioxide thin films measured by spectroscopic ellipsometry, Opt. Commun. **284**, 807 (2011).

[42] A. Gavinit and C. C. Y. Kwan, Optical properties of semiconducting VO_2 films, Phys. Rev. B **5**, 3138 (1972).

[43] X. Zhong, X. Zhang, A. Gupta, and P. LeClair, Avalanche breakdown in microscale VO_2 structures, J. Appl. Phys. **110**, 084516 (2011).

[44] C. N. Berglund and H. J. Guggenheim, Electronic properties of VO_2 near the semiconductor-metal transition, Phys. Rev. **185**, 1022 (1969).

[45] G. Dayal and S. A. Ramakrishna, Metamaterial saturable absorber mirror, Opt. Lett. **38**, 272 (2013).

[46] Y. Poochi, *Optical Waves in Layered Media*, J. W. Goodman (Wiley, New York, 1988).

[47] J. Joannopoulos, S. G. Johnson, J. N. Winn, and R. D. Meade, *Photonic Crystals Molding* the Flow of Light, 2nd ed. (Princeton University Press, Princeton, NJ, 2007).

[48] COMSOL MULTIPHYSICS, v. 5.2, www.comsol.com, COMSOL AB, Stockholm, Sweden.

[49] C. Cheng, K. Liu, B. Xiang, J. Suh, and J. Wu, Ultra-long, free-standing, single-crystalline vanadium dioxide micro/nanowires grown by simple thermal evaporation, Appl. Phys. Lett. **100**, 103111 (2012).

[50] E. Makri, H. Ramezani, T. Kottos, and I. Vitebskiy, Concept of a reflective power limiter based on nonlinear localized modes, Phys. Rev. A **89**, 031802(R) (2014).

[51] E. Makri, T. Kottos, and I. Vitebskiy, Reflective optical limiter based on resonant transmission, Phys. Rev. A **91**, 043838 (2015).

[52] J. H. Vella, J. H. Goldsmith, A. T. Browning, N. I. Limberopoulos, I. Vitebskiy, E. Makri, and T. Kottos, Experimental Realization of a Reflective Optical Limiter, Phys. Rev. Appl. **5**, 064010 (2016).